Catalysis Letters
https://doi.org/10.1007/s10562-018-2411-7

Metal Hexacyanometallate Nanoparticles: Spectroscopic Investigation on the Influence of Oxidation State of Metals on Catalytic Activity

Lisa K. Parrott[1] · **Elizabeth Erasmus**[1]

Received: 7 February 2018 / Accepted: 12 May 2018

Abstract

A series of metal hexacyanometallate nanoparticles K*x*M*y*[M′(CN)$_6$]*z*·*q*H$_2$O, with M=M′=Co (**1**) or Fe (**2**), M=Co and M′=Fe (**3**) and M=Fe and M′=Co (**4**) were prepared by either co-precipitation or reverse micro-emulsion. These nanoparticles were characterised by ATR FTIR, TEM and XPS, which revealed the presence of $Co^{II/III}$ and/or $Fe^{II/III}$ within the compounds. The average binding energies found for the Co $2p_{3/2}$ photoelectron lines for Co^{II} and Co^{III} were ca. 781.7 and 782.9 eV respectively, while the binding energies for Fe^{II} and Fe^{III} of the Fe $2p_{3/2}$ photoelectron lines were located at 709.5 and 711.4 eV. TEM reveal the particle size ranged between 180 and 520 nm. The eight different compounds' catalytic activity were tested for the solvent-free oxidation of benzyl alcohol using hydrogen peroxide as the oxidant. The progression of the reaction was monitored using ATR FTIR, by following the appearance of the carbonyl stretching frequency of the oxidation products, which showed the formation of not only benzyl aldehyde but also benzyl benzoate, which is the condensation product of benzyl alcohol and benzoic acid (another oxidation product). The TOF of the catalytic oxidation reaction was correlated with the mean particle diameter, % occurrence of $Co^{II/III}$ and/or $Fe^{II/III}$, total metal electronegativity and the degree of covalence of the Co- and Fe–ligand bond.

Graphical Abstract

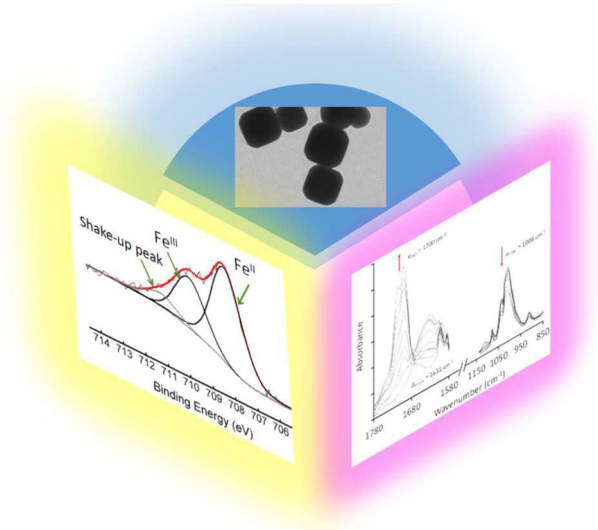

Keywords Hexacyanoferrate · Hexacyanocobaltate · XPS · Heterogeneous catalysts · Oxidation states

Electronic supplementary material The online version of this article (https://doi.org/10.1007/s10562-018-2411-7) contains supplementary material, which is available to authorized users.

Extended author information available on the last page of the article

Published online: 21 May 2018

1 Introduction

Transition metal hexacyanometallates are coordination complexes with a number of special physiochemical properties such as having the ability to accommodate two different transition metal ions within the same compound [1], and these two metals both have mixed valencies [2, 3], it can act as an electron transfer mediator [4], some show supermagnetism, [5], electrochromism [6], energy storage capability [7], and it is insoluble in water [8]. Even upon oxidation or reduction of the metals, the particles do not dissolve due to the zeolitic-like structure which allows for the movement of ions in and out to maintain neutrality of the compound [9]. Due to these and many other useful properties, transition metal hexacyanometallates have found applications in many different fields. One field that is not fully exploited is the use of metal hexacyanometallates as heterogeneous catalysts. There are reports available on the catalytic polymerization of ethylene oxide [10], manufacturing of polyether polyols [11], copolymerization of carbon dioxide and propylene oxide using metal hexacyanometallates [12]. As for the heterogeneous catalytic transformation of fine chemicals, the oxidation of alcohols have been reported [13, 14]. However, little is known about the effect of the different metals, the oxidation state of the metals or even particle size on the catalytic oxidation of alcohols. Here we report the preparation of metal hexcyanometallate nanoparticles by two different methods namely co-precipitation and reverse micro-emulsion to obtain nanoparticle of different sizes. A spectroscopic characterisation study was conducted to determine the percentage of the II and III oxidation state of both iron and cobalt. The influence of the variations of the spectroscopic data are related to the turn over frequency (TOF) of the heterogeneous catalytic oxidation benzyl alcohol using hydrogen peroxide as an oxidant.

2 Experimental

2.1 Synthesis of Nanoparticles

All solvents and solid reagents namely: potassium hexacyanocobaltate, potassium hexacyanoferrate(III), cobalt(II) chloride hexahydrate, anhydrous iron(III)chloride and dioctyl sulfosuccinate sodium salt (AOT) (purchased from Aldrich) were used as received. Distilled water was used in all procedures.

2.2 Co-precipitation Method

1a–4a were all prepared according to the same synthetic procedure, **1a** will be shown as an example.

2.3 Preparation of 1a

Potassium hexacyanocobaltate, $K_3[Co^{III}(CN)_6]$ (503 mg, 1.5 mmol) was dissolved in water (15 ml), creating an aqueous solution with a concentration of 0.1 M. To this cobalt-cyano- containing solution was added 15 ml of a 0.1 M aqueous solution of cobalt(II) chloride hexahydrate, $CoCl_2{\cdot}6H_2O$ (356 mg, 1.5 mmol). The resulting combined solution turned light pink and was stirred at room temperature for 15 min. Following this the solution was centrifuged at 8500 rpm for 30 min at 15 °C. The supernatant was discarded and the precipitate dried overnight in vacuo at 60 °C. The resulting purple powder was crushed to yield 0.301 g (93.7%) of pure **1a**.

ATR FTIR ν(C≡N)=2166 (M^{II}–CN–M'^{III}), 2052 (M^{II}–CN–M'^{II}) cm^{-1}.

XPS: Binding energy = 781.31 eV (Co^{II} $2p_{3/2}$); 782.59 eV (Co^{III} $2p_{3/2}$).

2.4 Characterisation Data for 2a

Yield 44.5% green powder

ATR FTIR ν(C≡N) = 2174 (M^{III}–CN–M'^{III}), 2166 (M^{II}–CN–M'^{III}) cm^{-1}.

XPS: Binding energy = 709.48 eV (Fe^{II} $2p_{3/2}$); 711.03 eV (Fe^{III} $2p_{3/2}$).

2.5 Characterisation Data for 3a

Yield 73.1% black powder

ATR FTIR ν(C≡N) = 2160 (M^{II}–CN–M'^{III}), 2108 (M^{II}–CN–M'^{II}) cm^{-1}.

XPS: Binding energy = 708.20 eV (Fe^{II} $2p_{3/2}$); 709.86 eV (Fe^{III} $2p_{3/2}$); 781.53 eV (Co^{II} $2p_{3/2}$); 783.01 eV (Co^{III} $2p_{3/2}$).

2.6 Characterisation Data for 4a

Yield 23.4% pale yellow powder

ATR FTIR ν(C≡N) = 2175 (M^{II}–CN–M'^{III}) cm^{-1}.

XPS: Binding energy = 709.66 eV (Fe^{II} $2p_{3/2}$); 711.17 eV (Fe^{III} $2p_{3/2}$); 781.89 eV (Co^{II} $2p_{3/2}$); 782.67 eV (Co^{III} $2p_{3/2}$).

2.7 Reverse Micro-emulsion Method

1b–4b were all prepared according to the same synthetic procedure, **1b** will be shown as an example. $M(AOT)_2$ with M=Co and Fe was prepared as described in Ref [15].

2.8 Preparation of 1b

Potassium hexacyanocobaltate, $K_3[Co^{III}(CN)_6]$ (664 mg, 2 mmol) was dissolved in a mixture of 2,2,4-trimethylpentane (10 ml) and water (10 ml). To this was added a solution of Na-AOT (450 mg, 1 mmol) dissolved in 2,2,4-trimethylpentane (10 ml), constituting Solution "A". Solution "B" was prepared by dissolving the previously prepared $Co(AOT)_2$ surfactant (2.289 g, 2.6 mmol) in 2,2,4-trimethylpentane (20 ml) and water (400 ml). Solution "A" was added dropwise to Solution "B" while stirring at room temperature for 15 min. The combined solution was sonicated for 15 min after which it was centrifuged (at 8500 rpm for 30 min at 15 °C). The clear supernatant was discarded and the precipitate washed with methanol to be centrifuged (at 8500 rpm for 30 min at 15 °C) again. The methanol supernatant was discarded and the pink precipitate was allowed to dry overnight in vacuo at 60 °C, yielding 252 mg (58.9%) of pure **1b**.

ATR FTIR $\nu(C{\equiv}N) = 2075$ (M^{II}–CN–M'^{II}) cm^{-1}.

XPS: Binding energy = 780.91 eV (Co^{II} $2p_{3/2}$); 782.59 eV (Co^{III} $2p_{3/2}$).

2.9 Characterisation Data for 2b

Yield 1.7% dark green powder

ATR FTIR $\nu(C{\equiv}N) = 2174$ (M^{III}–CN–M'^{III}) cm^{-1}.

XPS: Binding energy = 710.33 eV (Fe^{II} $2p_{3/2}$); 712.59 eV (Fe^{III} $2p_{3/2}$).

2.10 Charaterisation Data for 3b

Yield 15.3% brown-maroon powder

ATR FTIR $\nu(C{\equiv}N) = 2157$ (M^{II}–CN–M'^{III}), 2088 (M^{II}–CN–M'^{II}) cm^{-1}.

XPS: Binding energy = 708.49 eV (Fe^{II} $2p_{3/2}$); 710.44 eV (Fe^{III} $2p_{3/2}$); 781.41 eV (Co^{II} $2p_{3/2}$); 782.94 eV (Co^{III} $2p_{3/2}$).

2.11 Charaterisation Data for 4b

Yield 0.2% pale yellow powder

ATR FTIR $\nu(C{\equiv}N) = 2175$ (M^{III}–CN–M'^{III}), 2082 (M^{II}–CN–M'^{II}) cm^{-1}.

XPS: Binding energy = 710.73 eV (Fe^{II} $2p_{3/2}$); 713.50 eV (Fe^{III} $2p_{3/2}$); 781.92 eV (Co^{II} $2p_{3/2}$); 782.84 eV (Co^{III} $2p_{3/2}$).

2.12 Characterisation

Infrared spectra of neat samples were recorded with a Thermo Scientific IR spectrometer and NICOLET iS50 ATR attachment, running OMNIC software (Version 9.2.86).

2.13 X-ray Photoelectron Spectroscopy

XPS data was recorded on a PHI 5000 Versaprobe system, with a monochromatic Al Kα X-ray source. Powered samples were mounted on the sample holder by means of carbon tape. Spectra were obtained using the aluminium anode (Al Kα = 1486.6 eV), operating at 50 µm, 12.5 W and 15 kV energy (97 X-ray beam). A low energy neutraliser electron gun was used to minimise charging of the samples. The instrument work function was calibrated to give a binding energy of 284.8 eV for the lowest binding energy peak of the carbon 1s envelope, corresponding to adventitious carbon. Survey scans were recorded at constant pass energy of 187.85 eV, while detailed region scans were recorded at constant pass energy of 29.35 eV for C and O, and 93.90 eV for the metals, with an energy step of 0.1 eV; the analyzer resolution is ≤ 0.5 eV. Charge neutralisation was enhanced by shooting the mounted sample with an Ar gun during data recording. The resolution of the PHI 5000 Versaprobe system is FWHM = 0.53 eV at a pass energy of 23.5 eV and FWHM = 1.44 eV at a pass energy of 93.90 eV. The background pressure was 2×10^{-8} mbar. Spectra have been charge corrected to the main line of the carbon 1s spectrum, which was set to 284.8 eV. XPS data was analysed utilising Multipak version 8.2c computer software [16], and applying Gaussian/Lorentz fits (the Gaussian/Lorentz ratios were always > 95%). The photoelectron lines were charge corrected against the lowest binding energy of the fitted adventitious C 1s peak at 284.8 eV (the normal position of C–C according to the XPS Handbook [16]).

2.14 Transmission Electron Microscopy

Transmission electron microscopy (TEM) was performed with a Phillips (FEI) CM100 equipped with a Megaview III digital camera and coupled to an Oxford X-Max (80 nm^2), energy-dispersive X-ray spectroscope (EDS). The digital images were analysed utilizing Soft Imaging System (analySIS) software. Multiple dispersions were prepared by mixing the powder with methanol and deposited on a 300-mesh nickel grid. Digital images were obtained after preparation.

2.15 Heterogeneous Catalytic Oxidation of Benzyl Alcohol

A mixture of benzyl alcohol (5.2 ml, 50 mmol) and 0.030 g of the catalyst (either **1–4**) were heated till reflux while stirring. Hydrogen peroxide (2.3 ml, 96.7 mmol) was added with the evolution of gas (bubbling occurred). Small samples were periodically remove for ATR FTIR analysis to follow the progression of the reaction.

3 Results and discussion

Metal hexacyanometallate nanoparticles which has a general formula of K*x*M*y*[M′(CN)$_6$]*z*·*q*H$_2$O, with *x, y, z* and *q* representing stoichiometric numbers and M=M′=Co (**1**) or Fe (**2**), M=Co and M′=Fe (**3**) and M=Fe and M′=Co (**4**) were prepared by two different methods. The first method is a simple co-precipitation reaction which involves the mixing of the water soluble starting materials, a metal halide and the potassium hexacyanometallate at room temperature in ambient air. This resulted in the formation of the water-insoluble metal hexacyanometallates (**1a**–**4a**). The yields obtained from co-precipitation ranged from 23% (**4a**) to 93% (**1a**).

The second method forms a surfactant stabilized nanoparticle utilising the anionic surfactant sodium bis(2-ethylhexyl)sulfosusuccinate (Na-AOT). This allowed for the confinement of the synthesis to occur in nanoscale droplets, an additional measure to ensure the formation of nanoparticles. The preparation involves the vigorous mixing of two micro-emulsions, the surfactant metal salt (M(AOT)$_2$ with M=Co or Fe) [15] and the potassium hexacyanometallate surfactant-containing solution. This resulted in a milky but colourful fine suspension, which indicates that the exchange of cations between different droplets (of the two different micro-emulsions) are sufficient to activate nucleation and growth. Yields obtained for the reverse micro emulsion procedure were very low (ranging between 0.2–58.9%).

Infra-red spectroscopy is useful to distinguish between different functional groups within a sample. Stretching frequencies of hydroxyl groups (*ν*OH) can be identified between 3650 and 3100 cm^{-1} [17], cyanide groups (*ν*C≡N) between 2300 and 2000 cm^{-1} [18, 19], cyanates (*ν*-NCO) at ca. 2250 cm^{-1} [20], metal-bound carbon monoxide (*ν*C≡O) between 1900 and 2200 cm^{-1} [21, 22], while carbonyls stretching frequencies (*ν*CO) can be found between 1600 and 1800 cm^{-1} [23, 24]. Factors such as the electronic influence of the chemical surroundings also affects the wavenumber of the stretching frequency of the functional group [17].

The ATR FTIR spectra of the metal hexacyanometallates and their starting materials are shown in the Figures S1–S5, in the Supplementary Information. From the ATR FTIR spectra of **1–4** revealed the presence of water within the samples, adsorbed on the outside as well as being trapped in the inside of the zeolite-structure of the metal hexacyanometallates. The OH stretching frequency (*ν*OH) of water adsorbed on the outside of the structure is located at ca. 3600–3100 cm^{-1}, while the δHOH bending vibration of the coordinated water molecules which are trapped inside the structure in the intercalated positions can be detected at ca. 1600 cm^{-1} [25]. With the exception if **1b** and **4a**, two peaks were observed in the characteristic cyanide stretching frequency area. Since it is known that shifts in vibration frequencies is an indicator of different oxidation of the metal to which the CN is bound, the different peaks were assigned to the different possible M$^{II/III}$–CN–M′$^{II/III}$ chains in correlation to published reports [18, 19], and the data summarised in Table 1.

To further characterise the metal hexacyanometallate nanoparticles, X-ray Photoelectron Spectroscopy (XPS) was conducted. The binding energy measured of each element corresponds with the atomic potential which provides insight into the oxidation status as well as the chemical and electronic environment of the element [26–31].

In the survey scans of all the compounds C, N, O, Fe, Co and K were detected. All the binding energies of the photoelectron spectra were referenced against the lowest binding

Table 1 The ATR FTIR measured stretching frequencies detected for **1a**–**4b**

Compound	No.	*ν*C≡N (cm^{-1}) M^{III}–CN–M′^{III}	*ν*C≡N (cm^{-1}) M^{II}–CN–M′^{III}	*ν*C≡N (cm^{-1}) M^{II}–CN–M′^{II}	*ν*OH (cm^{-1}) Absorbed outside	δHOH (cm^{-1}) Intercalated
Co–CN–Co	**1a**		2166	2052	3287	1605
	1b			2075	3328	1586
Fe–CN–Fe	**2a**	2174	2166		3369	1605
	2b	2174			3389	1607
Fe–CN–Co	**3a**		2160	2108	3367	1601
	3b		2157	2088	3379	1608
Co–CN–Fe	**4a**	2175			3195	1604
	4b	2175		2082	3338	1586

energy of the C–C simulated adventitious C 1s photoelectron line, which was set at 284.8 eV [16]. The carbon of nanoparticles, M–**C**≡N–M′ was measured at ca. 288 eV, while the N 1s photoelectron line from the –C≡**N**– group is located at ca. 398 eV (see Figure S6).

Figure 1 shows the detail scan of Fe 2p and Co 2p area, including the simulated peak fittings, of **3a** as an example. The XPS data of the metal hexacyanometallates, **1a**–**4b**, with respect to the N 1s, Fe $2p_{3/2}$ and Co $2p_{3/2}$ photoelectron lines are presented in Table 2.

Both the Fe $2p_{1/2}$ and Fe $2p_{3/2}$ photoelectron lines of the iron-containing compounds, **2–4**, shows splitting of the photoelectron line into two sharp well-defined peaks (see Fig. 1 top), which is assigned to Fe^{II} and Fe^{III} (at the higher binding energy). The Fe $2p_{3/2}$ photoelectron lines assigned to Fe^{II} have an average binding energy of ca. 709.5 eV (see Table 2), with a spin orbit splitting between the Fe $2p_{3/2}$ and Fe $2p_{1/2}$ photoelectron lines of ca. 12.9 eV. Whereas the Fe $2p_{3/2}$ photoelectron lines assigned to Fe^{III} is located at a binding energy of ca. 711.4 eV (see Table 2), an average of 1.9 eV higher than the Fe^{II}. The average atomic ratio (AR) between the amount of Fe^{II} and Fe^{III} present is 2.1:1 (see Table 2). The Fe 2p photoelectron lines are slightly asymmetric towards the high energy side, where a small shake-up peak could be fitted at ca. 2.8 eV higher than the main Fe 2p envelope.

The calculated average binding energy for the Fe^{II} (709.5 eV) correlates good with published values for the binding energy of the Fe^{II} within ferrocene anchored onto an aminoalkyl silane-capped silicon-wafer (709.7 eV) [32]. While the calculated average binding energy for the Fe^{III} (711.4 eV) was found to be slightly higher than reported data for iron(III) tris(β-diketonato) complexes (710.9 eV) [57], but in good agreement with sodium iron(III) oxide (711.5 eV) [33], and iron(III) chloride (711.3 eV) [34].

The detail scans of the cobalt Co 2p photoelectron lines, did not show the Co^{II} and Co^{III} as separate peaks like the iron. However, a small shoulder is clearly present on the low energy side, while the photoelectron line is asymmetric in shape towards the high energy side. The Co 2p photoelectron lines were fitted with three simulated peaks (see Fig. 1 bottom left). The simulated fit of the Co $2p_{3/2}$ photoelectron lines were assigned in order from the low energy side: Co^{II} at a binding energy of ca. 781.7 eV, Co^{III} at a binding energy of ca. 782.9 eV (see Table 2), and the last simulated peak at ca. 787.2 eV is a shake-up peak. The allocation correlates well with the 781.7 eV reported for Co^{II} in a bimetallic carboxylate complex spin-coated onto a Si-wafer [35], and the 782.4 eV reported for Co^{III} in CoF_3 [34]. The average atomic ratio between the amount of Co^{II} and Co^{III} present is 2.1:1 (see Table 2).

Using the atomic ratios obtained between the potassium, cobalt and/or iron, as well as the relative % of the oxidation states from the XPS, it is possible to derive the a quantified stoichiometric formula for **1–4** in the form of $K_xM_y[Fe(CN)_6]_z$:

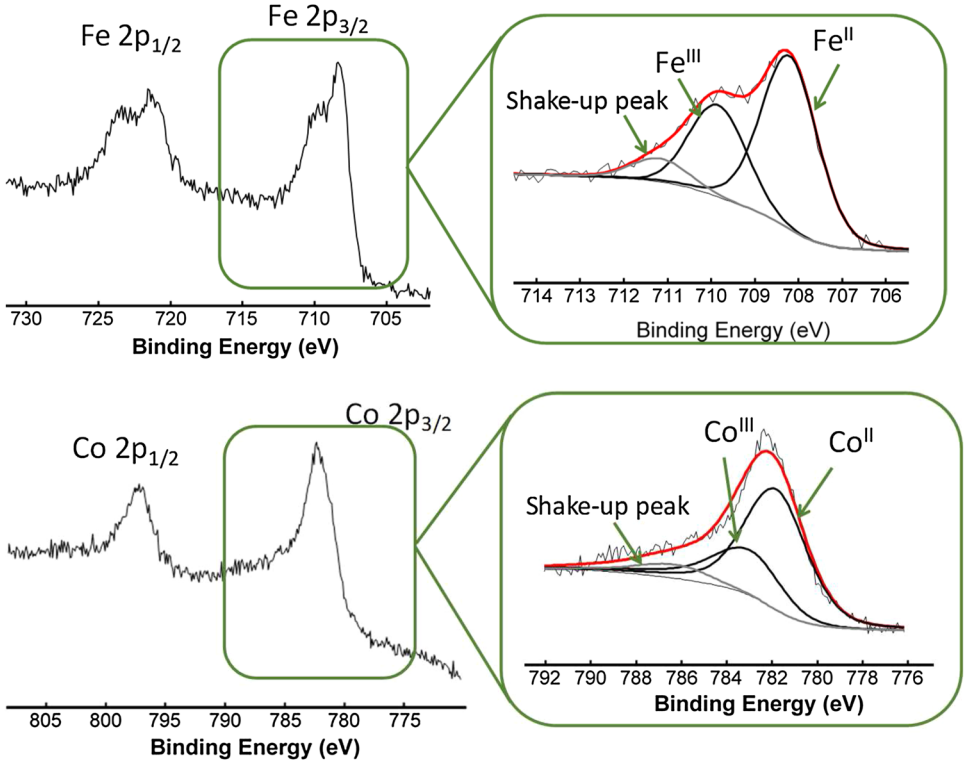

Fig. 1 XPS detail scans of the Fe 2p (top) and Co 2p areas of **3a**

Table 2 Binding energies (eV) of N 1s photoelectron line, the Fe $2p_{3/2}$ photoelectron line of Fe^{II} and Fe^{III}, the Co $2p_{3/2}$ photoelectron line of Co^{II} and Co^{III}

	BE N 1s (eV)	BE Fe^{II} $2p_{3/2}$ (eV)	BE Fe^{III} 2p3/2 (eV)	BE Co^{II} $2p_{3/2}$ (eV)	BE Co^{III} 2p3/2 (eV)
F2	397.84	708.61			
F3	398.03		710.08		
C3	398.87				786.79
1a	398.06			781.31 (63.6%)	782.59 (36.3%)
AR	2.8			1	
1b	397.68			780.91 (70.9%)	782.59 (29.1%)
AR	3.2			1	
2a	398.92	709.48 (66.7%)	711.03 (33.3%)		
AR	4.6	1			
2b	397.90	710.33 (73.8%)	712.59 (26.2%)		
AR	3.5	1			
3a	398.02	708.20 (66.1%)	709.86 (33.8%)	781.53 (79.9%)	783.01 (20.1%)
AR	3.9	1		1	
3b	398.27	708.49 (72.1%)	710.44 (27.9%)	781.41 (33.4%)	782.94 (66.6%)
AR	5.3	1.2		1	
4a	398.39	709.66 (66.7%)	711.17 (33.3%)	781.89 (74.6%)	782.67 (25.4%)
AR	5.3	1		1.3	
4b	398.12	710.73 (70.1%)	713.50 (29.9%)	781.92 (40.3%)	782.84 (59.7%)
AR	5.4	1.1		1	

The atomic ratios (AR) and % occurrence (given in brackets) are also presented. F2 = $K_3(Fe^{II}(CN)_6)$; F3 = $K_3(Fe^{III}(CN)_6)$ and C3 = $K_3(Co^{III}(CN)_6)$

- **1a**: $K_{0.7}Co_{0.4}[Co(CN)_6]_1$
- **1b**: $K_{0.9}Co_{0.7}[Co(CN)_6]_1$
- **2a**: $K_{1.5}Fe_{0.7}[Fe(CN)_6]_1$
- **2b**: $K_{1.1}Fe_{0.75}[Fe(CN)_6]_1$
- **3a**: $K_{1.3}Co_1[Fe(CN)_6]_1$ or $K_{1.3}Co^{II}{}_{0.8}/Co^{III}{}_{0.2}[Fe^{II}{}_{0.66}/Fe^{III}{}_{0.34}(CN)_6]_1$
- **3b**: $K_{0.97}Co_{1.69}[Fe(CN)_6]_1$ or $K_{0.97}Co^{II}{}_{0.87}/Co^{III}{}_{0.33}[Fe^{II}{}_{0.33}/Fe^{III}{}_{0.67}(CN)_6]_1$
- **4a**: $K_{1.2}Fe_{0.8}[Co(CN)_6]_1$ or $K_{1.2}Fe^{II}{}_{0.5}/Fe^{III}{}_{0.3}[Co^{II}{}_{0.75}/Co^{III}{}_{0.25}(CN)_6]_1$
- **4b**: $K_{1.2}Fe_{1.1}[Co(CN)_6]_1$ or $K_{1.2}Fe^{II}{}_{0.78}/Fe^{III}{}_{0.32}[Co^{II}{}_{0.40}/Co^{III}{}_{0.6}(CN)_6]_1$

The Transmission electron microscopy (TEM) images of **1a** and **b**, the cobalt hexacyanocobaltate nanoparticle prepared respectively by co-precipitation and reverse micro-emulsion are shown in Fig. 2 as examples. The mean particle distribution (nm) of **1–4** range between ca. 180 nm (for **3b**) and 520 nm (for **3a**), and are summarised in Table 3. The size depends on the different metals as well as the preparation method. In general, it was found that the nanoparticles prepared by reverse micro-emulsion are slightly smaller. The shape and size detected by TEM image are similar to the variety of Prussian blue analogues (including iron hexacyanocobaltate (Fe–Co) and manganese-iron hexacyanocobaltate ($Mn_{0.5}Fe_{0.5}$–Co), which is comparable with **1a**–**b**) prepared by a "co-polymer-co-morphology" concept using PVP [36]. This shows that it is possible to obtain similar shape using different methods of preparation.

Considering the physical properties such mixed valencies, high surface area, insolubility (making the metals self-supporting) of metal hexacyanometallates, which are all favourable for utilisation as a heterogeneous catalyst, the catalytic

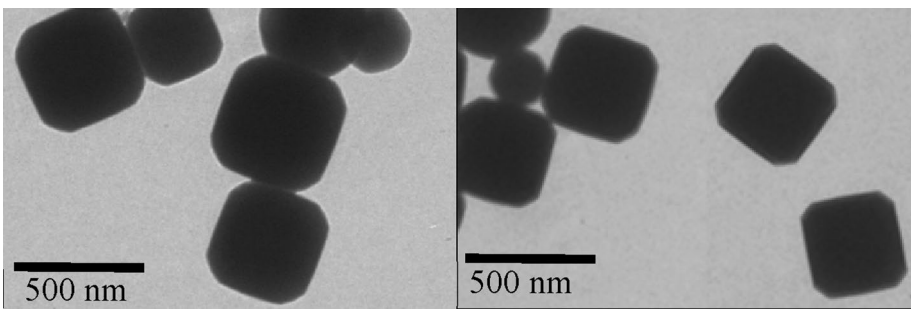

Fig. 2 TEM image of the nanoparticles of (left) cobalt hexacyanocobaltate (**1a**) prepared by co-precipitation and (right) cobalt hexacyanocobaltate (**1b**) prepared by reverse micro-emulsion (right)

Table 3 Summary of the TOF (determined from catalysis), the pseudo first order rate constant (k_{obs} as determine from following the kinetic of the catalysis process), mean diameter (from TEM) and oxidation state ratio of the Fe and Co (from XPS) in **1–4**

Compound	No.	TOF (h^{-1})	kobs (h^{-1})	Combined metal EN	Mean diameter (nm)	% Fe^{II}	% Fe^{III}	% Co^{II}	% Co^{III}
Co–CN–Co	**1a**	88	0.744	6.723	278			63.6	36.3
	1b	95	1.076	6.467	316			70.9	29.1
Fe–CN–Fe	**2a**	65	0.871	6.071	438	66.7	33.3		
	2b	122	1.651	5.900	187	73.8	26.2		
Fe–CN–Co	**3a**	48	0.510	6.109	521	66.1	33.8	79.9	20.1
	3b	128	1.667	6.885	181	72.1	27.9	33.4	66.6
Co–CN–Fe	**4a**	78	0.889	6.202	274	66.7	33.3	74.6	25.4
	4b	119	1.433	6.783	271	70.1	29.9	40.3	59.7

activities of **1–4** was tested for the solvent-free oxidation of benzyl alcohol using the environmentally friendly oxidant hydrogen peroxide [14].

The progression of the catalytic reaction was monitored using Attenuated Total Reflection Fourier Transformed Infrared (ATR FTIR) analysis, see Fig. 3. From the ATR FTIR spectra the formation of the oxidation products bearing a carbonyl (C=O) groups could be detected following the appearance of the characteristic FTIR stretching frequency at ca. 1700 cm^{-1}. This approach could also be used to monitor the consumption of the starting material, the benzyl alcohol, by following the disappearance of the carbon-hydroxy C–O–H stretching frequency at 1006 cm^{-1}.

Closer inspection of the carbonyl stretching frequency (νCO) revealed that it consisted of two overlapping peaks at 1698 and 1715 cm^{-1}, see Fig. 3 Left. The carbonyl stretching frequency at 1698 cm^{-1} started as the favourable product but as the reaction progressed the oxidation product with a νCO at 1715 cm^{-1} started to appear. This is on contrast to what was observed by Ali et al. who found benzaldehyde as the only oxidation product [14].

Determination of the oxidation products responsible for the carbonyl stretching frequencies observed at 1698 and 1715 cm^{-1}, were identified by comparison to commercially available benzaldehyde and benzoic acid. From the results obtained of the commercial samples, the νCO at 1698 cm^{-1} was assigned to benzaldehyde, however no carbonyl stretching frequency for benzoic acid (which appeared at 1676 cm^{-1}) could be detected in the FTIR spectra of the oxidation products (see Fig. 3 Right). However, the νCO at 1715 cm^{-1} obtained from the oxidation product was detected at the same the carbonyl stretching frequency of commercially available benzyl benzoate, located at 1718 cm^{-1} (see Fig. 3 Left).

Since benzyl benzoate is the condensation product formed between benzyl alcohol and benzoic acid, it is implied that benzoic acid must have formed and that the characteristic

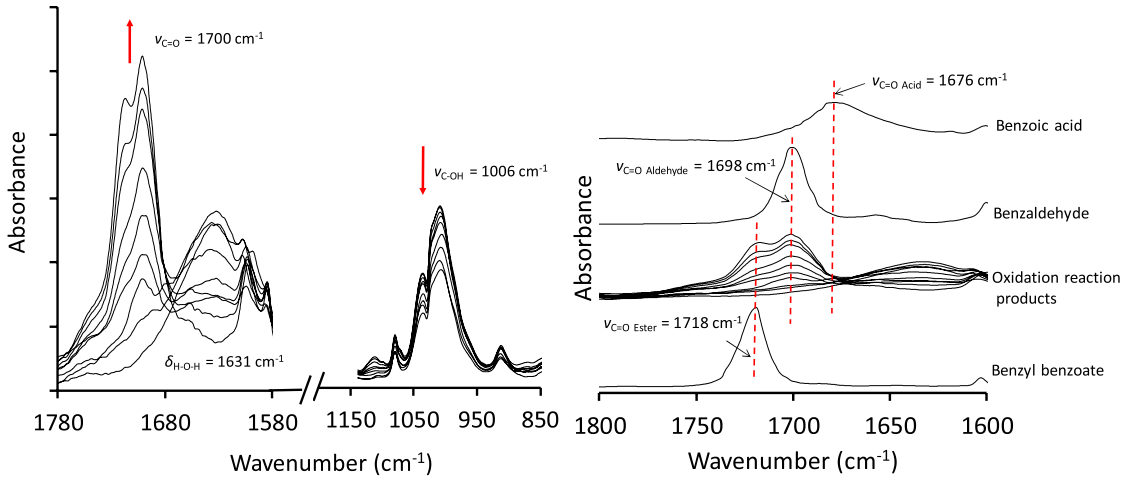

Fig. 3 Left: ATR FTIR spectra sections showing the appearance and disappearance of stretching frequencies at 1698 and 1006 cm^{-1} over time of the solvent-free catalytic oxidation of benzyl alcohol using the environmentally friendly oxidant H_2O_2 using **4b** as the heterogeneous catalyst. Right: Comparative ATR FTIR spectra of the carbonyl stretching frequency area showing from top to bottom benzoic acid, benzaldehyde, the progress of the catalytic reaction and benzyl benzoate

carbonyl stretching frequency is probably hidden underneath the water peak or that as soon as the benzoic acid is formed it condenses with the benzyl alcohol to form benzyl benzoate. The formation of this series of oxidation products (benzaldehyde, benzoic acid and benzyl benzoate) along with the formation of toluene (not detectable/distinguishable from ATF FTIR) has been reported in literature [37].

From the data collected for the solvent-free catalytic oxidation of benzyl alcohol using hydrogen peroxide as the oxidant over **1–4**, the turn over frequencies (TOF) were calculated after 180 min and summarised in Table 3.

The turn over frequencies (TOF) was calculated after 180 min using Eq. 1. The amount of molecules converted was determined using the intensity ratio between the *ν*CO (at 1698 cm^{-1}) for benzaldehyde and *ν*C–OH (at 1006 cm^{-1}) for benzyl alcohol. From a calibration curve the percentage aldehyde/alcohol (% convertion) present after 180 min could be measured (see Figure S7). Using data of catalyzed by **4b** as an example, after 180 min (3 h) the intensity ratio between *ν*CO:*ν*C–OH = 1.8. From the calibration curve it is measured that ca. 78% of the molecules converted. Since the catalytic reaction was started with 50 mmol (3.011×10^{22} molecules) benzyl alcohol and 78% of the molecules converted, the amount of molecules converted is 2.3×10^{22}. Considering that ca. 1.1×10^{-4} mol (30 mg) of catalyst was added to the reaction, the amount of active sites present is ca. 6.6×10^{19}. Thus the TOF (for **4b**) = $[(2.3\times10^{22}/6.6\times10^{19})/3\text{ h}]\approx119\text{ h}^{-1}$ or 1.99 min^{-1}.

$$\text{TOF} = \frac{\left(\frac{\text{amount of molecules converted}}{\text{amount of active sites}}\right)}{\text{time in h}} \quad (1)$$

The TOF of **1–4** ranged between 48 h^{-1} (for **3a**) and 122 h^{-1} (for **2b**), which is comparable to 123 h^{-1} reported in literature [14]. The TOF of the catalyst with the same composition e.g. Fe–CN–Co **3a** (48 h^{-1}) and **3b** (128 h^{-1}) varied significantly. To determine the cause of this variation as well as to determine other factors influencing the TOF, relationships were established between the TOF and mean particle diameter, % occurrence of the different oxidation states of Fe and Co, combined metal electronegativity and the degree of covalence of the metal–ligand bonds (see Figs. 4, 5).

In general, as the mean particle diameter of the nanoparticles decreased, the TOF of the catalytic solvent-free oxidation of benzyl alcohol increased (Fig. 4 Left), which is consistent with many data reported on literature on various catalytic systems [38–41]. Even though the metal hexacyanometallate systems are not normal supported catalyst, but self-supporting catalyst, the smaller particles exposes more active metal sites to the surface giving rise to the higher TOF.

The metal hexacyanometallates are a combination of different metals (for **3–4**) with each metal also having different oxidation states namely II and III, which would influence the TOF differently. The influence of the % occurrence of the II and III oxidation state of both Fe and Co on the TOF is shown in Fig. 4 Middle and Right. Inversely proportional relationships were obtained for the correlation between TOF and % occurrence of Fe^{III} and Co^{II}, while directly proportional relationships were found for the correlation between TOF and % occurrence of Fe^{II} and Co^{III}. This shows that a higher % occurrence of Fe^{II} and Co^{III} increases the TOF, while a higher % occurrence of Fe^{III} and Co^{II} decreases the TOF. The % occurrence of Fe^{II} and Fe^{III} does not play as big a role in TOF as Co oxidation state as can be seen from the slope of the graphs.

Seeing as it is well reported that oxidation reaction utilising H_2O_2 as an oxidant according the Fenton mechanism starts with a Fe^{II} source as the catalyst [24, 42, 43], the higher TOF found by the higher % occurrence of Fe^{II} thus is expected. A number of results published the use of homogenous $Co^{II/III}$ and $Fe^{II/III}$ complexes for oxidation reactions. It has been indicated that the use of a homogenous Fe^{III}

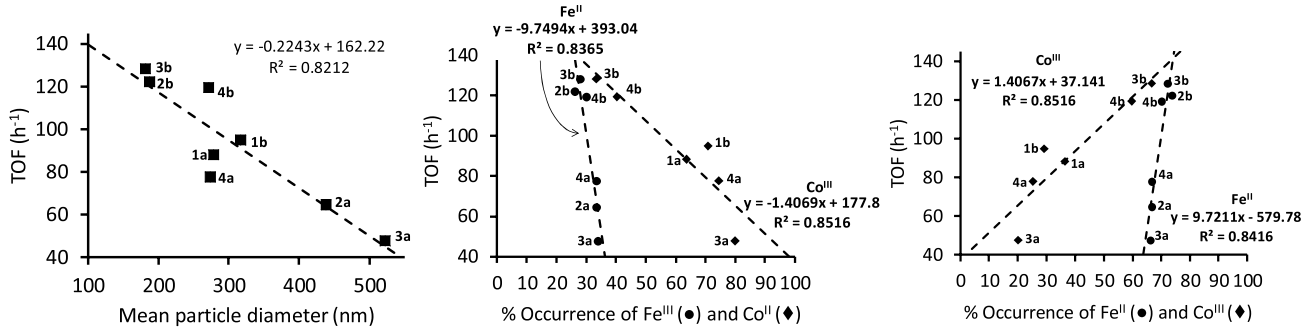

Fig. 4 Left: Relationship between the Mean particle diameter (as determined from TEM) and the TOF (as determined from the catalysis) of **1–4**. Middle: Relationship between the % occurrence of Fe^{III} (●) and Co^{II} (♦), as determined from XPS, and the TOF (as determined from the catalysis) of **1–4**. Right: Relationship between the % occurrence of Fe^{II} (●) and Co^{III} (♦), as determined from XPS, and the TOF (as determined from the catalysis) of **1–4**

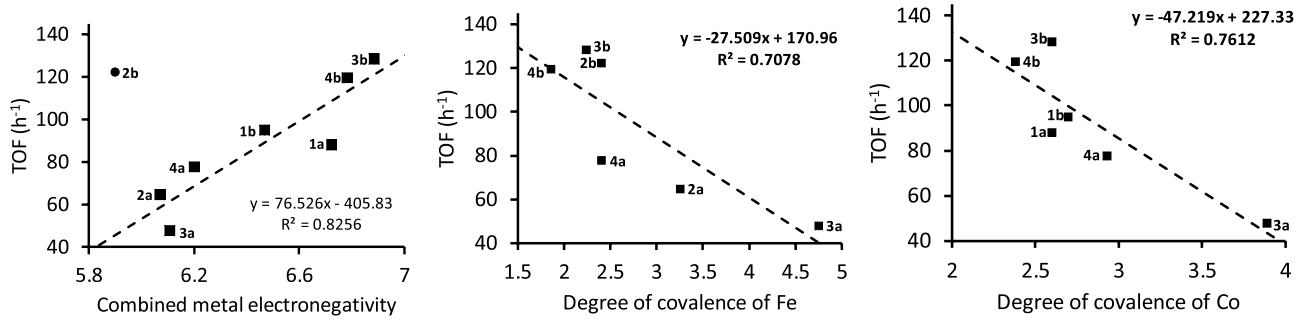

Fig. 5 Left: Relationship between the Total electronegativity and the TOF (as determined from the catalysis) of **1–4**. Middle: Relationship between the degree of covalence of the Co (an indication from XPS) and the TOF (as determined from the catalysis) of **1–4**. Right: Relationship between the degree of covalence of the Fe (an indication from XPS) and the TOF (as determined from the catalysis) of **1–4**

complex having the same ligand system than its Co^{II} counterpart is superior in its catalytic activity for the oxidation of alcohols [44], and the use of a Co^{II} Schiff base complex has also been reported to need the addition of a bromide ion as promotor [45, 46]. All confirming that the variation in the % occurrence of Fe has a smaller effect on the oxidation than the % occurrence of Co.

There are numerous reports available on how the electronegativity of molecular fragments influences the physical properties of the compounds. For instance, many linear relationships have been established to indicate the dependence of physical properties such as reaction rates [47], oxidation potentials [48–52], binding energies [53–57] on electronegativity, using the Gordy scale group electronegativity of molecular fragments. Electronegativity also influence TOF and since it is known that electronic environment of metals also influence the catalytic activity [61], an attempt was made to demonstrate how the electronegativity of **1–4** influence the TOF. However, seeing as the Gordy group electronegativity scale (scale used for organic molecular fragments) could not be used, the electronegativity of metal ions as determined by Li et al. [58] was used. A combined metal electronegativity for each compound (**1–4**) was determined using the following equation:

$$\left[\left(\%\ \text{occurrence of Fe}^{II}\right)\times\left(\text{EN of Fe}^{II}\right)\right]+\left[\left(\%\ \text{occurrence of Fe}^{III}\right)\times\left(\text{EN of Fe}^{III}\right)\right]+\left[\left(\%\ \text{occurrence of Co}^{II}\right)\times\left(\text{EN of Co}^{II}\right)\right]+\left[\left(\%\ \text{occurrence of Co}^{III}\right)\times\left(\text{EN of Co}^{III}\right)\right]$$

The % occurrence of each oxidation state for each metal was obtained from XPS (Table 2) and the electronegativity (EN) of each metal ion is: EN of $Fe^{II}=2.636$, EN of $Fe^{III}=3.835$, EN of $Co^{II}=2.706$ and EN of $Co^{III}=4.520$ [58]. For compounds **1** and **2**, having only Co and Fe respectively, the calculated combined metal electronegativity was doubled to compensate for the fact that only two types of metal ions are present within one compound where as **3** and **4** has four types of metal ions are present within one compound (see Table 3). With the exception of **2b**, a directly proportional relationship was displayed between the combined metal electronegativity and the TOF. Thus, the more electronegative compounds resulted in higher TOF's. The normal Fenton mechanism involves the oxidation of the Fe^{II} and the reduction in Fe^{III} by hydrogen peroxide, where the net effect is the disproportionation of H_2O_2 to produce.

two different radicals ($HO^{\cdot}$ and $HOO^{\cdot}$) and water. It can be deduced that the more electronegative (more electron poor) the compound in totality, the easier it is to disproportionate hydrogen peroxide, causing the higher TOF.

It is known that the shake-up peak (satellite peak) of metal photoelectron lines in XPS represents the charge transfer process and the separation (in eV) between the main and shake-up peak is a measure of the degree of covalence of the metal–ligand bond [59]. The lower the degree of covalence of a metal–ligand bond, the more "ionic" character will be displayed by the bond. An inversely proportional relationship was established between degree of covalence of the metal–ligand bond (for both Fe and Co) and the TOF (see Fig. 5 middle and right).

Though the degree of covalence of the metal–ligand bond is not the same as the metal–ligand bond strength it is a feature of molecular orbital energy [59], which corresponds to bond strength (the higher the molecular orbital energy the higher the bond strength). Considering this, the inversely proportional relationship found for the degree of covalence of the metal–ligand bond and TOF is consistent with reported data. During catalytic oxidation reactions using metal oxides, the M–O bond strength has been reported to be an important factor influencing the catalytic reaction [60, 61]. An inversely proportional relationship exist between M–O bond strength and catalytic activity,

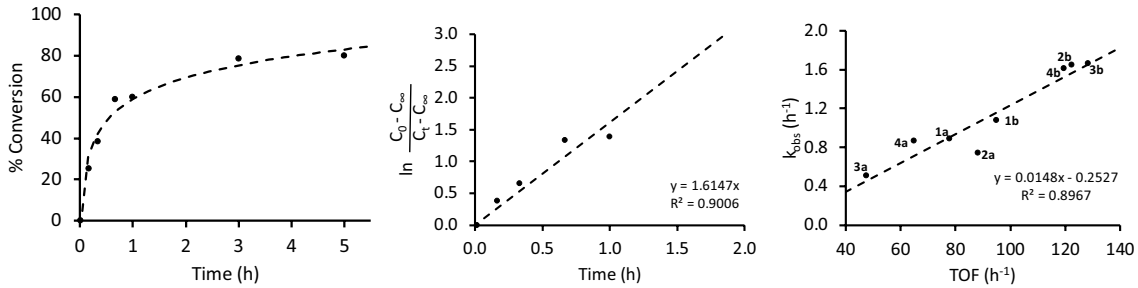

Fig. 6 Left: Time trace showing the conversion of benzyl alcohol to its oxidation products at 25 °C using H_2O_2 as oxidant and **4b** as the catalyst. Middle: A kinetic plot of data for this process that leads to the observed first order rate constant k_{obs}. Right: Relationship between the TOF and the k_{obs} measure during the catalytic oxidation of benzyl alcohol using **1–4** as the catalysts

which is consistent with our findings. When the M–O bond strength is high the catalytic activity is low, up to a point where the M–O bond strength is so strong that the catalyst could be inactive. While a weak bond strength could lead to total and even over oxidation.

The kinetics of the catalytic oxidation of benzyl alcohol to benzaldehyde was also investigated (further oxidation to the acid and ester was not investigated). Figure 6 (Right) shows the kinetic time trace of the formation of benzaldehyde using using H_2O_2 as oxidant and **4b** (as an example) as the catalyst. The graph in Fig. 6 (Middle) confirms that the behavior of the catalytic reaction is "pseudo" first-order and the slope of this graph corresponds to the observed rate constant (k_{obs}) for the reaction under solvent free conditions at 25 °C. The % conversion as well as the observed rate constant (k_{obs}) for the catalytic oxidation reaction using reaction **1–4** are summarised in Table 3.

Comparison of the TOF with the k_{obs} value (Fig. 6 Right), revealed a directly proposional relationship, the higher TOF the higher the k_{obs}.

4 Conclusion

Based on the spectroscopic characterisation (ATR FTIR and XPS) of the metal hexacaynometallates, **1–4**, in combination with the correlation studies on the effect of mean particle diameter, % occurrence of $Co^{II/III}$ and/or $Fe^{II/III}$, total metal electronegativity and the degree of covalence of the Co- and Fe–ligand bond on the catalytic activity, it is clarified that smaller particles with a high % Fe^{II} and Co^{III} content, a high total metal electronegativity and a low degree of covalence produces the best self-supporting metal hexacyanometallate catalyst for the oxidation of benzyl alcohol under solvent-free oxidation using H_2O_2 as oxidant.

Acknowledgements The author would like to acknowledge generous financial support from Sasol and UFS during the course of this study.

References

1. Gutiérrez-Becerra A, Martínez-Martínez F, Bárcena-Soto M, Casillas N, Ceja I, Prévost S, Gradzielski Z, Escalante JI (2014) Coll Surf A 444:63
2. Zhang K, Kang S, Yao ZS, Nakamura K, Yamamoto T, Einaga Y, Azuma N, Miyazaki Y, Nakano M, Naegawa S, Sato O (2016) Angew Chem Int Edt 55:6047
3. Lee E, Seong S, Kim HW, Kim DH, Thakur N, Yusuf SM, Kim B, Min BI, Kim Y, Kim JY, de Groot FM, Kang JS (2017) Phys Chem Rev B 96:195120
4. Shirakawa T, Higashi M, Tomita O, Abe R (2017) Sustain Energy Fuels 1:1065
5. Catala L, Gacoin T, Boilot JP, Riviere E, Paulsen C, Lhotel E, Mallah T (2003) Adv Mat 15:826
6. De Longchamp DM, Hammond PT (2004) Chem Mater 16:4799
7. Qiu X, Liu Y, Wang L, Fan LZ (2018) Appl Surf Sci 434:1285
8. Ishizaki M, Sakamoto M, Tanaka H, Kawamoto T, Kurihara M (2011) Mol Crys Liq Crys 539:18
9. Kulesza PJ, Malik MA, Berettoni M, Giogetti M, Zamponi S, Schmidt R, Marassi R (1998) J Phys Chem B 102:1870
10. Le-Khac B (1997) US 5 637 673
11. Chen S, Xu NP, Shi J (2004) Prog Org Coat 49:125
12. Chen S, Hua ZJ, Fang Z, Qi GR (2004) Polymer 45:6519
13. Ali SR, Bansal VK, Khan AA, Jain SK, Ansari MA (2009) J Mol Catal A 303:60
14. Ali SR, Chandra P, Latwal M, Jain SK, Bansal VK, Singh SP (2011) Chin J Catal 32:1844
15. Eastoe J, Fragneto G, Robinson BH, Towey TF, Heenan RK, Leng FJ (1992) J Chem Soc Faraday Trans 88:461
16. Moulder F, Stickle WF, Sobol PE, Bomben KD (1995) Handbook of X-ray photoelectron spectroscopy. ULVAC-PHI, Inc., Enzo, Chigasaki
17. Erasmus E (2016) Hemij Indus 70:595
18. Berrettoni M, Ciabocco M, Fantauzzi M, Giorgetti M, Rossi A, Caponetti E (2015) RSC Adv 5:35435
19. Gerber SJ, Erasmus E (2018) Mat Chem Phys 203:73
20. Conradie MM, Conradie J, Erasmus E (2014) Polyhedron 79:52
21. Erasmus E (2016) Inorg Chim Acta 451:197
22. Erasmus E (2016) Polyhedron 106:18
23. Erasmus E, Conradie J, Muller A, Swarts JC (2007) Inorg Chim Acta 360:2277

24. Erasmus E, Claassen JO, van der Westhuizen WA (2016) Water SA 42:442
25. Sheha RR (2012) J Coll Interf Sci 338:21
26. Buitendach BE, Erasmus E, Landman M, Niemantsverdriet JW, Swarts JC (2016) Inorg Chem 55:1992
27. Jansen van Rensburg A, Landman M, Erasmus E, van der Westhuizen D, Ferreira H, Conradie MM, Conradie J (2016) Electrochim Acta 219:204
28. van As A, Joubert CC, Buitendach BE, Erasmus E, Conradie J, Cammidge AN, Chambrier I, Cook MJ, Swarts JC (2015) Inorg Chem 54:5329
29. Jansen van Rensburg A, Landman M, Conradie MM, Erasmus E, Conradie J (2017) Electrochim Acta 246:897
30. Jansen van Rensburg A, Landman M, van Rooyen PH, Conradie MM, Erasmus E, Conradie J (2017) Polyhedron 133:307
31. Gostynski R, Fraser R, Landman M, Erasmus E, Conradie J (2017) J Organomet Chem 836:62
32. Trzebiatowska-Gusowska M, Gagor A, Coetsee E, Erasmus E, Swart HC, Swarts JC (2013) J Organomet Chem 745::393
33. Allen GC, Curtis MT, Hooper AJ, Tucker PM (1974) J Chem Soc Datlon Trans 14:1525
34. Carver JC, Schweitzer GK, Carlson TA (1972) J Phys Chem 57:973
35. Erasmus E, Niemantsverdriet JW, Swarts JC (2012) Langmuir 28:16477
36. Li X, Yaun L, Wang J, Jiang L, Rykov AI, Nagy DL, Bogdan C, Ahmed MA, Zhu K, Sun G, Yang W (2015) Nanoscale. https://doi.org/10.1039/C5NR07193C
37. Nowicka E, Hofmann JP, Parker SF, Sankar M, Lari GM, Kondrat SA, Knight DW, Bethell D, Weckhuysen BM, Hutchings GJ (2013) Phys Chem Chem Phys 15:12147
38. Bond GC (1985) Surf Sci 156:966
39. Anderson JR (1985) Sci Prog 69:461
40. Zahmakiran M, Philippot K, Ozkar S, Chaudet B (2012) J Chem Soc Dalton Trans 41:590
41. Suchorski Y, Drachsel W (2007) Top Cat 46:201
42. Lee C (2015) Enviro Eng Res 20:205
43. Yong F, Deli W, Luming M (2013) Prog Chem 25:1219
44. Sahu D, Banik B, Borah M, Das P (2014) Lett Org Chem 11:671
45. Sharma VB, Jain SL, Sain BJ (2005) Mol Catal A 227:47
46. Partheimer W (2006) Adv Synth Catal 348:559
47. Erasmus E (2014) J Electroanal Chem 727:1
48. Muller TJ, Conradie J, Erasmus E (2012) Polyhedron 33:257
49. Erasmus E (2011) Inorg Chim Acta 378:95
50. Erasmus E, Swarts JC (2013) New J Chem 37:2862
51. Erasmus E (2016) Polyhedon 106:18
52. Erasmus E, Muller AJ, Siegert U, Swarts JC (2016) J Organomet Chem 821:62
53. Erasmus E (2018) J Elec Spec Rel Phen 223:84
54. Gostynski R, Conradie J, Erasmus E (2017) RSC Adv 7:27718
55. Erasmus E (2017) S Afr J Chem 70:94
56. Liu R, Conradie J, Erasmus (2016) J Elec Spec Rel Phen 206:46
57. Conradie J, Erasmus E (2016) Polyhedron 119:142
58. Li K, Li M, Xue D (2012) J Phys Chem A 116:4192
59. Buitendach BE, Erasmus E, Niemantsverdriet JW, Swarts JC (2016) Molecules 21:1427
60. Grasselli RK (2014) Catal Today 238:10
61. Vedrine JC (2016) Catal 6:22

Affiliations

Lisa K. Parrott[1] · Elizabeth Erasmus[1]

✉ Elizabeth Erasmus
erasmuse@ufs.ac.za

[1] Department of Chemistry, University of the Free State, Bloemfontein 9300, South Africa